The Astrophysical Journal, 864:38 (12pp), 2018 September 1 https://doi.org/10.3847/1538-4357/aad3c9

CO (7−6), [C I] 370 μm, and [N II] 205 μm Line Emission of the QSO BRI 1335-0417 at Redshift 4.407

Nanyao Lu[1,2], Tianwen Cao[1,2,3], Tanio Díaz-Santos[4], Yinghe Zhao[5,6,7], George C. Privon[8,9,10], Cheng Cheng[1,2,11], Yu Gao[12], C. Kevin Xu[1,2], Vassilis Charmandaris[13,14], Dimitra Rigopoulou[15], Paul P. van der Werf[16], Jiasheng Huang[1,2], Zhong Wang[1,2], Aaron S. Evans[17,18], and David B. Sanders[19]

[1] National Astronomical Observatories, Chinese Academy of Sciences (CAS), Beijing 100012, People's Republic of China; nanyao.lu@gmail.com
[2] China-Chile Joint Center for Astronomy, Camino El Observatorio 1515, Las Condes, Santiago, Chile
[3] School of Astronomy and Space Science, University of Chinese Academy of Sciences, Beijing, People's Republic of China
[4] Nucleo de Astronomia de la Facultad de Ingenieria, Universidad Diego Portales, Av. Ejercito Libertador 441, Santiago, Chile
[5] Yunnan Observatories, Chinese Academy of Sciences, Kun-ming 650011, People's Republic of China
[6] Key Laboratory for the Structure and Evolution of Celestial Objects, Chinese Academy of Sciences, Kunming 650011, People's Republic of China
[7] Center for Astronomical Mega-Science, CAS, 20A Datun Road, Chaoyang District, Beijing 100012, People's Republic of China
[8] Department of Astronomy, University of Florida, 211 Bryant Space Sciences Center, Gainesville, 32611 FL, USA
[9] Departamento de Astronomía, Universidad de Concepción, Casilla 160-C, Concepción, Chile
[10] Pontificia Universidad Católica de Chile, Instituto de Astrofisica, Casilla 306, Santiago 22, Chile
[11] Instituto de Física y Astronomía, Universidad de Valparaíso, Avda. Gran Bretanã 1111, Valparaíso, Chile
[12] Purple Mountain Observatory, CAS, Nanjing 210008, People's Republic of China
[13] Department of Physics, University of Crete, GR-71003 Heraklion, Greece
[14] IAASARS, National Observatory of Athens, GR-15236, Penteli, Greece
[15] Department of Physics, University of Oxford, Keble Road, Oxford OX1 3RH, UK
[16] Leiden Observatory, Leiden University, P.O. Box 9513, 2300 RA Leiden, The Netherlands
[17] Department of Astronomy, University of Virginia, 530 McCormick Road, Charlottesville, VA 22904, USA
[18] National Radio Astronomy Observatory, 520 Edgemont Road, Charlottesville, VA 22903, USA
[19] University of Hawaii, Institute for Astronomy, 2680 Woodlawn Drive, Honolulu, HI 96822, USA
Received 2018 March 6; revised 2018 July 10; accepted 2018 July 13; published 2018 August 29

Abstract

We present the results from our Atacama Large Millimeter/submillimeter Array (ALMA) imaging observations of the CO(7−6), [C I] 370 μm (hereafter [C I]), and [N II] 205 μm (hereafter [N II]) lines and their underlying continuum emission of BRI 1335-0417, an infrared bright quasar at $z = 4.407$. At the achieved resolutions of $\sim$1.″1 to 1.″2 (or 7.5–8.2 kpc), the continuum at 205 and 372 μm (rest frame), the CO(7−6), and the [C I] emissions are at best barely resolved whereas the [N II] emission is well resolved with a beam-deconvolved major axis of 1.″3 (±0.″3) or 9(±2) kpc. As a warm dense gas tracer, the CO(7−6) emission shows a more compact spatial distribution and a significantly higher peak velocity dispersion than the other two lines that probe lower density gas, a picture favoring a merger-triggered star formation (SF) scenario over an orderly rotating SF disk. The CO(7−6) data also indicate a possible QSO-driven gas outflow that reaches a maximum line-of-sight velocity of 500–600 km s^{-1}. The far-infrared (FIR) dust temperature ($T_{\rm dust}$) of 41.5 K from a graybody fit to the continuum agrees well with the average $T_{\rm dust}$ inferred from various line luminosity ratios. The resulting $L_{\rm CO(7-6)}/L_{\rm FIR}$ luminosity ratio is consistent with that of local luminous infrared galaxies powered predominantly by SF. The $L_{\rm CO(7-6)}$-inferred SF rate is 5.1(±1.5) × $10^3\,M_\odot$ yr^{-1}. The system has an effective star-forming region of $1.7^{+1.7}_{-0.8}$ kpc in diameter and a molecular gas reservoir of $\sim 5 \times 10^{11}\,M_\odot$.

Key words: galaxies: active – galaxies: ISM – galaxies: star formation – infrared: galaxies – ISM: molecules – submillimeter: galaxies

1. Introduction

As more and more galaxies have been identified at high redshifts from recent deep photometric surveys, with some quasars (QSO) and other emission-line galaxies discovered at extremely high redshifts of $z > 7$ (e.g., Finkelstein et al. 2013; Watson et al. 2015; Hu et al. 2017; Venemans et al. 2017; Bañados et al. 2018), how to effectively characterize their star formation (SF) rate (SFR), SFR surface density ($\Sigma_{\rm SFR}$), and interstellar gas properties becomes an acute and yet challenging task. In particular, a direct measurement of $\Sigma_{\rm SFR}$ is difficult due to a requirement for high spatial resolution.

Among the high-z galaxy samples studied so far (see Carilli & Walter 2013 for a review), there is a population of the so-called submillimeter (submm) galaxies (SMGs) at $z \gtrsim 2$, first identified in submm bands (Blain et al. 2002). SMGs are among the brightest star-forming galaxies in the early universe (Casey et al. 2014). However, their large distances and dusty nature make it difficult to sufficiently reveal their internal SF structures at kiloparsec to subkiloparsec scales. As a result, it is still debatable whether their enormous bolometric luminosity is driven by a galaxy major merger, i.e., a scaled-up version of local ultra-luminous infrared galaxies (ULIRGs; with a total 8–1000 μm luminosity, $L_{\rm IR} > 10^{12}\,L_\odot$; e.g., Tacconi et al. 2006, 2008), or by a rotating, star-forming galaxy disk that is constantly fueled by the larger quantities of gas available at high-z via an increased cold gas accretion rate (e.g., Agertz et al. 2009; Dekel et al. 2009; Davé et al. 2010).

Lu et al. (2015) presented a simple spectroscopic approach for simultaneously inferring the SFR, $\Sigma_{\rm SFR}$ and some molecular gas properties of a distant galaxy by measuring only the fluxes of the CO(7−6) line (rest frame 806.652 GHz or 372 μm) and either the

[N II] line at 205 μm (1461.134 GHz; hereafter as [N II]) or the [C II] line at 158 μm (1900.56 GHz; hereafter as [C II]). For local luminous infrared galaxies (LIRGs; $L_{\rm IR} > 10^{11}\,L_{\odot}$) and ULIRGs, the CO(7−6) line luminosity, $L_{\rm CO(7-6)}$, can be used to infer the SFR of a galaxy with ∼30% accuracy, irrespective of whether the galaxy hosts an active galactic nucleus (AGN; Lu et al. 2014, 2015, 2017a; Zhao et al. 2016a). Furthermore, the steep anticorrelation between the [N II]/CO(7−6) (or [C II]/CO (7−6)) luminosity ratio and the rest-frame far-infrared (FIR) color, $C(60/100)$ ($\equiv f_{\nu}(60\ \mu{\rm m})/f_{\nu}(100\ \mu{\rm m})$), can be used to estimate $C(60/100)$ or the dust temperature $T_{\rm dust}$ (Lu et al. 2015). $C(60/100)$ is in turn related to $\Sigma_{\rm SFR}$ (Liu et al. 2015; Lutz et al. 2016). Alternatively, one can estimate $C(60/100)$ from the [C I]/CO(7−6) luminosity ratio (Lu et al. 2017a; also see the Appendix), where [C I] refers to the fine-structure transition ($^3P_2 \rightarrow {}^3P_1$) at 370 μm (809.342 GHz) of neutral carbon. The frequency separation between the [C I] and CO(7−6) lines is only $2.69/(1+z)$ GHz at redshift z. This greatly increases observational efficiency as both lines can fit within the same sideband of the Atacama Large Millimeter/submillimeter Array (ALMA; Wootten & Thompson 2009). These indirect approaches to estimating $\Sigma_{\rm SFR}$ are useful at high redshifts, where it is often challenging to resolve a galaxy in the FIR/submm.

In addition, these gas cooling lines probe different interstellar gas phases. With a critical density ($n_{\rm crit}$) of $\sim 10^5\,{\rm cm}^{-3}$ and an excitation temperature ($T_{\rm ex}$) of ∼150 K (Carilli & Walter 2013), the CO(7−6) line probes dense and warm molecular gas that is energetically associated with and in the proximity of current or very recent SF activities (Lu et al. 2014, 2017a). The [C I] line has $n_{\rm crit} \sim 10^3\,{\rm cm}^{-3}$, similar to that of the CO(1−0) line (Carilli & Walter 2013). Recent observations suggest that this line traces general molecular gas as the CO(1−0) line does (e.g., Papadopoulos & Greve 2004; Papadopoulos et al. 2004; Jiao et al. 2017; Lu et al. 2017a). The [N II] line has a low $n_{\rm crit} \sim 50\,{\rm cm}^{-3}$ (Carilli & Walter 2013) for collisional excitation with electrons. This line probes mainly diffuse, hot ionized gas (Zhao et al. 2016b; Díaz-Santos et al. 2017).

A hallmark of a galaxy major merger is the molecular gas funneled into the inner region of the merging galaxies (Sanders et al. 1988; Solomon & Sage 1988; Scoville et al. 1989; Sanders & Mirabel 1996; Solomon et al. 1997; Downes & Solomon 1998; Gao & Solomon 1999; Evans et al. 2002) as a result of gravitational torque during the merger (Barnes & Hernquist 1996; Hopkins et al. 2009). Furthermore, the nonaxisymmetric tidal force also leads to gas turbulences and shocks that compress the gas into higher densities (e.g., Bournaud et al. 2011). Recent cosmological simulations of galaxy mergers at high z (e.g., Sparre & Springel 2016) suggest that different gas phases have different spatial distributions, with (a) star-forming dense gas in the inner region of the merging galaxies, and (b) diffuse hot ionized gas extending to large radii. The region between (a) and (b) is dominated by (c) gas of intermediate densities. In this merger scenario, the CO(7−6) line predominantly traces the gas phase (a); the [N II] would be particularly sensitive to the gas phase (b). Likely, the [C I] could have a significant contribution from the gas phase (c). Such spatial scale differences are indeed observed in some local advanced mergers between, for example, CO(6−5) and a low-J CO line such as CO(1−0) or CO(2−1) (e.g., Xu et al. 2014, 2015). On the other hand, in an orderly rotating disk SF scenario, the SF occurs in the dense blobs embedded in the gaseous disk. As a result, both CO(7−6) and [C I] may reflect the same disk geometry and kinematics.

In this paper, we present the results from our ALMA observations of the CO(7−6), [C I], and [N II] line emission of BRI 1335-0417, an infrared luminous QSO at $z = 4.407$ (Storrie-Lombardi et al. 1994), as part of our continued effort to expand the number of $z > 4$ galaxies with CO(7−6), [C I], [N II], and [C II] detections. The host galaxy system of this unlensed QSO (Storrie-Lombardi et al. 1996) is dusty and gas rich (Omont et al. 1996; Guilloteau et al. 1997; Benford et al. 1999; Carilli et al. 1999, 2002; Yun et al. 2000; Wagg et al. 2014; Jones et al. 2016) and is likely going through a major merger involving two galaxy progenitors roughly along the north–south direction, separated by about 0.″6 (∼4 kpc; Riechers et al. 2008). The QSO, likely hosted by the dominant southern galaxy member, has an estimated black hole mass of $\sim 6 \times 10^9\,M_{\odot}$ (Shields et al. 2006). The detection of the CO(5−4) emission (Guilloteau et al. 1997) indicates a large amount of warm and dense molecular gas associated with the on-going intense SF. The ALMA data presented here allow for not only some quantitative characterization of the SF and gas properties, but also further testing of the galaxy merger scenario for this system, which is caught at the stage of active assembling of a massive galaxy and rapid growth of the central massive black hole when the universe was only ∼1.4 billion years old.

In the remainder of this paper, we describe our observations, data reduction, and results in Section 2, analyze the observed line and dust continuum emission, quantify the SF and gas properties, and discuss merger-dominated SF scenario in Section 3, and finally summarize our results in Section 4. Throughout the paper, we use a flat cosmology with $\Omega_M = 0.27$, $\Omega_{\Lambda} = 0.73$, and $H_0 = 71\ {\rm km\,s^{-1}\,Mpc^{-1}}$. At $z = 4.407$, the luminosity distance is 40,993 Mpc and 1″ corresponds to 6.8 kpc.

2. Observations and Results

2.1. Observations and Data Reduction

The CO(7−6)/[C I] observation of BRI 1334-0417 was carried out in the ALMA Band 4 in the time division mode (TDM) in two equal-duration runs on 2016 March 4 and 19, respectively. The observation utilized 39 of the 12 m antennas with baselines ranging from 15 to 460 m. The effective total on-target integration is 607 s. The separate ALMA band-6 [N II] observation was conducted in TDM in one session on 2016 January 4, with an on-target integration of 303 s. A total of 40 of the 12 m antennas were used, with baselines from 15 to 331 m. In each observation, 1 of the 4 spectral windows (SPWs), each of 1875 MHz wide, was used to cover the redshifted line(s), and the other 3, tuned at some nearby frequencies on both sides of the spectral line, were used for the continuum measurement. Each SPW has 128 channels with a channel width of 15.625 MHz. The effective spectral resolution is 31.25 MHz, equivalent to 63 and 35 km s^{-1} for the CO(7−6)/[C I] and [N II] observations, respectively. The CO(7−6) and [C I] lines are covered by the same SPW as the two lines are separated by only 0.50 GHz ($=2.69\ {\rm GHz}/(1+z)$). The pointing, phase, bandpass, and flux calibrations were based on Ganymede, J1116+0829, J1332-0509, and J1337-1257 in the CO(7−6)/[C I] observation and on J1337-1257 and J1332-0509 in the [N II] observation.

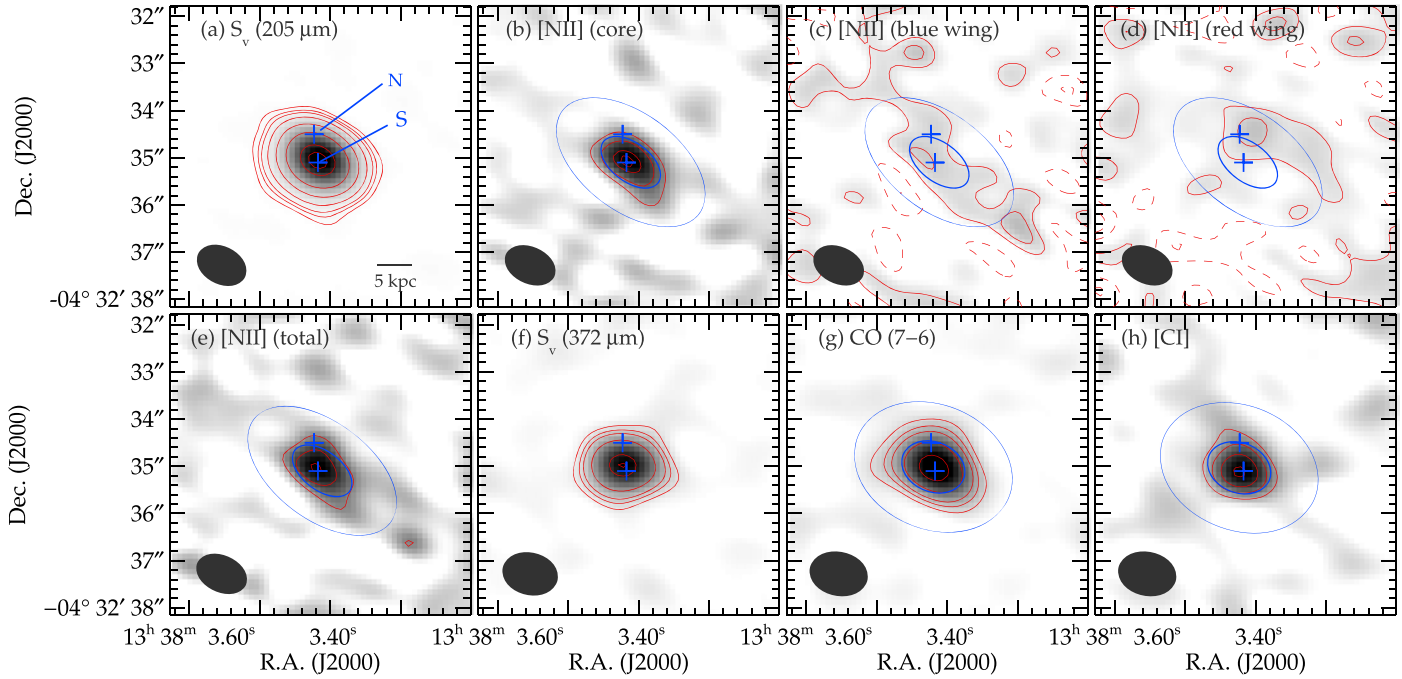

Figure 1. Surface brightness images: (a) the continuum at ∼205 μm (rest frame); the [N II] line emission integrated over (b) the core frequency range from 270.021 to 270.472 GHz (243 to −257 km s^{-1}), (c) the blue wing (270.472–270.742 GHz or −257 to −557 km s^{-1}), (d) the red wing (269.751 to 270.021 GHz or 543 to 243 km s^{-1}), or (e) the full frequency range from 269.751 to 270.742 GHz; (f) the continuum at ∼372 μm (rest frame); (g) the CO(7−6) emission integrated from 148.902 to 149.449 GHz (543 to −557 km s^{-1}); and (h) the [C I] 370 μm emission integrated from 149.499 to 149.847 GHz (320 to −377 km s^{-1}). In each panel, the image and the red contours refer to the same data; the image stretch is from 0 to the highest contour plotted except for panels (c) and (d), in which the gray scales are the same as in panel (b). All the contours start at 3σ, except for those in panels (c) and (d). In units of mJy beam^{-1}, the contours are shown at [3, 5, 7, 12, 24, 48, 96, 120] × 0.057 in (a) or at [3, 5, 7, 12, 24, 27.6] × 0.038 in (f). In units of Jy km s^{-1} beam^{-1}, the contours in (b), (e), (g), and (h) are plotted at [3, 5, 7, 7.7] × 0.11, [3, 5, 6.4] × 0.17, [3, 5, 7, 12, 19] × 0.12, and [3, 5, 7, 9] × 0.092, respectively. The contours in both (c) and (d) are at [−2, −1, 1, 2] × σ, where σ = 0.08 Jy km s^{-1} beam^{-1}, and the contours of negative values are shown by the dashed line. The black ellipse at the lower left corner in each panel indicates the relevant (FWHM) synthesized ALMA beam. The blue ellipses in each line image indicate, respectively, the two apertures used for extracting the 1D spectra in Figure 3. The two blue crosses in each panel mark the locations of sources N and S (see the text). The 5 kpc scale is shown in panel (a).

The data reduction was carried out with the Common Astronomy Software Applications (CASA) 4.5.3 and the final images were cleaned using the Briggs weighting with the parameter "robust" = 0, resulting in a synthesized beam of full width at half maximum (FWHM) of 1.″2 × 0.″9 (1.″1 × 0.″8) at a position angle (PA; N to E) of 82° (64°) for the CO(7−6)/[C I] ([N II]) observation. The rms noise in the final continuum image is ∼38 (57) μJy beam^{-1} from the CO(7−6) ([N II]) observation. For the spectral cube data, the continuum was removed using the CASA function "uvcontsub" of order = 1. We further reduced the channel width of the final spectral cube to 100 km s^{-1}, resulting in an rms noise of ∼0.29 (0.37) mJy beam^{-1} for the CO(7−6)/[C I] ([N II]) data.

2.2. Results

We show in Figure 1 the two continuum images as well as the frequency-integrated line images. For the [N II] emission, the spatially integrated line profile shows possible high-velocity components (as analyzed in Section 3.3). We therefore include in Figure 1 four separate frequency-integrated images for the [N II] emission: a "core" image (Figure 1(b)) that encompasses the main emission component, two images representing the blue (Figure 1(c)) and red (Figure 1(d)) wing components, respectively, and a "total" image (Figure 1(e)) that was integrated over the full frequency range. In each panel, the two blue crosses mark the respective positions of the two main gas components resolved in the Very Large Array (VLA) CO(2−1) map in Riechers et al. (2008). These two sources (hereafter referred to as sources N and S) are separated by ∼200 km s^{-1} along the line of sight and by ∼0.″6 (∼4 kpc) spatially. As shown by Riechers et al., these individual sources are rich in molecular gas and likely represent the progenitors in an ongoing major galaxy merger.

We fit a 2D Gaussian function to each of the images in Figure 1, except for the image panels (b) through (d). The resulting central position, FWHM major and minor axes, and PA are given in Table 1. Based on these results, the continuum emission at 205 and 372 μm (rest frame) are both unresolved or just barely resolved, as well as the CO(7−6) and [C I] emission. In contrast, the [N II] emission appears to be well resolved, with an ALMA beam-deconvolved major axis ($d_{\rm deconv}$) of 1.″3 (±0.″4) (9 ± 3 kpc) as discussed in more detail in Section 3.3.

Figure 2 compares the moment-1 and moment-2 images of the emission lines using the CASA function "immoments" on all the channel data points above 2.5σ, where σ is the pixel-to-pixel noise per frequency channel (i.e., spaxel). In addition, we used only the channels free from contamination by another spectral line. Therefore, these surface brightness-weighted images show mainly the inner galaxy. All moment-1 images indicate a similar overall velocity field, with a roughly north–south velocity gradient of up to ∼150 km s^{-1}. There are subtle differences between the lines: for example, the velocity field increases to +50 km s^{-1} toward a southwest patch in the moment-1 image of the CO(7−6) line. However, this patch completely disappears if the spaxel S/N cutoff is raised to S/N > 3.5. Therefore, these subtle differences are of low detection significance. In contrast, the moment-2 images reveal

Table 1
Observed and Derived Parameters[a]

Parameter	Value
Observations:	
ALMA beam ($\nu_{\rm obs} \approx 149$ GHz)	($1\farcs2 \times 0\farcs9$, 82°)
ALMA beam ($\nu_{\rm obs} \approx 270$ GHz)	($1\farcs1 \times 0\farcs8$, 64°)
Continuum:	
Gaussian fit position[b] (J2000)	($13^{\rm h}38^{\rm m}03\fs419$, −4°32′35.″06)
Gaussian fit size[c] (149 GHz)	$1\farcs20(\pm0\farcs04) \times 0\farcs96(\pm0\farcs03)$, 89°(±6°)
S_ν (149 GHz) (mJy)	1.17 (±0.07)
Gaussian fit size[c] (270 GHz)	$1\farcs18(\pm0\farcs01) \times 0\farcs92(\pm0\farcs01)$, 61°(±1°)
S_ν (270 GHz) (mJy)	9.03 (±0.11)
CO(7−6)[d]:	
Gaussian fit position (J2000)	($13^{\rm h}38^{\rm m}03\fs420$, −4°32′35.″05)
Gaussian fit size[c]	$1\farcs34(\pm0\farcs06) \times 0\farcs97(\pm0\farcs04)$, 67°(±5°)
Central frequency (GHz)	149.179 (±0.003)
FWHM (km s^{-1})	341 (±11)
Flux (Jy km s^{-1})	3.08 (±0.11)
[C I][d]:	
Gaussian fit position (J2000)	($13^{\rm h}38^{\rm m}03\fs424$, −4°32′35.″03)
Gaussian fit size[c]	$1\farcs38(\pm0\farcs15) \times 1\farcs06(\pm0\farcs12)$, 68°(±17°)
Central frequency (GHz)	149.690 (±0.004)
FWHM (km s^{-1})	314 (±16)
Flux (Jy km s^{-1})	1.04 (±0.09)
[N II][d] (total):	
Gaussian fit position (J2000)	($13^{\rm h}38^{\rm m}03\fs412$, −4°32′35.″09)
Gaussian fit size[c]	$1\farcs70(\pm0\farcs32) \times 0\farcs92(\pm0\farcs14)$, 49°(±9°)
Central frequency (GHz)	270.24 (±0.03)
FWHM (km s^{-1})	603 (±64)
Flux (Jy km s^{-1})	1.95 (±0.23)
[N II][d] (3-Gaussian fit)[e]:	
Frequency (core) (GHz)	270.27 (±0.01)
FWHM (core) (km s^{-1})	238 (±31)
Flux (core) (Jy km s^{-1})	1.04 (±0.14)
Frequency (red side) (GHz)	269.93 (±0.05)
FWHM (red side) (km s^{-1})	394 (±109)
Flux (red side) (Jy km s^{-1})	0.62 (±0.18)
Frequency (blue side) (GHz)	270.58 (±0.02)
FWHM (blue side) (km s^{-1})	147 (±49)
Flux (blue side) (Jy km s^{-1})	0.34 (±0.12)
Line and continuum luminosities:	
$L_{\rm [N\ II],total}/L_\odot$	$9.2(\pm1.1) \times 10^8$
$L_{\rm [N\ II],core}/L_\odot$	$4.9(\pm0.7) \times 10^8$
$L_{\rm CO(7-6)}/L_\odot$	$8.0(\pm0.3) \times 10^8$
$L_{\rm [C\ I]}/L_\odot$	$2.7(\pm0.2) \times 10^8$
$L_{\rm [C\ II]}$[f]$/L_\odot$	$1.6(\pm0.3) \times 10^{10}$
$L_{\rm FIR}$[g]$/L_\odot$	$2.0(\pm0.1) \times 10^{13}$

Notes.
[a] ALMA flux uncertainties cited do not include the absolute calibration uncertainty likely at ∼10%. The uncertainties of the continuum flux and source size based on a 2D Gaussian fit to an image were estimated following the prescription in Condon (1997) for correlated noise cases. The uncertainties for the parameters from a Gaussian fit to a spectrum were estimated following the formulae in Lenz & Ayres (1992).
[b] Taken from the 2D Gaussian fit to the 270 GHz continuum image that has a higher S/N between the two continuum images. The measured position difference between the two continuum bands is $0\farcs09$. The typical astrometric accuracy of our ALMA observations is $\sim0\farcs1$.
[c] FWHM major and minor axes, followed by the major axis PA (N to E), from the 2D Gaussian fit.
[d] Spectrum extracted from within an elliptical aperture that resembles the FWHM ellipse of the 2D Gaussian fit to the frequency-integrated line image, but with the major and minor axes each stretched by a factor of $n = 2.5$. For the CO(7−6) and [C I] lines, we used a common aperture referenced to the 2D Gaussian fit to the [C I] image.
[e] These are three Gaussian components from the fit to the [N II] spectrum in Figure 3(c).
[f] Based on the [C II] flux in Wagg et al. (2010).
[g] The quoted luminosity error reflects how much the fitted SED-based $L_{\rm FIR}$ varies if $T_{\rm dust}$ changes from 41.5 K by ±2 K.

significant differences between the lines: the [N II] line shows a smoothly varying velocity dispersion that is up to 80 km s^{-1} over the inner galaxy except for a higher value in a region at ∼1.″1 southwest of source S. Upon closer examination of the spectral cube, this region of apparently higher velocity dispersion is likely caused by a redshifted (at −185 km s^{-1}) signal detected only at S/N ∼ 3, which has no clear corresponding signal in the other two lines. By comparison, the CO(7−6) emission shows a more patchy velocity dispersion field with an elongated area at PA ∼ 45° showing higher velocity dispersions of 150–180 km s^{-1}. This patchiness remains identifiable until the spaxel S/N cutoff is raised to S/N > 5 in constructing the moment images. For the [C I] line, a peak velocity dispersion of ∼120 km s^{-1} is seen around source S. Therefore, the dense molecular gas traced by CO (7−6) is effectively subject to a higher turbulent velocity field than the gas component traced by either [C I] or [N II]. It is thus unlikely that the CO(7−6) and [C I] line emission arise from the same region. We analyze this further in Section 3.2 and discuss its physical implications in Section 3.6.

Figure 3 shows the extracted 1D spectra using an elliptical aperture of the size index $n = 2.5$ (upper panels) or $n = 1.0$ (lower panels), where the index n refers to the common stretching factor for the major and minor axes of the aperture relative to that of a reference aperture ($n = 1$), with the aperture PA always fixed. Therefore, the two apertures used in Figure 3 differ in their major and minor axes by a common scaling factor of 2.5/1.0. For the spectra encompassing the CO(7−6) and [C I] lines (left panels in Figure 3), the aperture of $n = 1.0$ is defined by having its FWHM major and minor axes and PA set to the corresponding values in the 2D Gaussian fit result for the [C I] line in Table 1; for the [N II] spectrum (right panels in Figure 3), it is set to the 2D Gaussian fit result for the total [N II] image in Table 1. These $n = 1.0$ and $n = 2.5$ apertures are also plotted in Figures 1 and 2.

We fit a Gaussian function to each spectral line in Figure 3 and the results are shown by the black curves. The [N II] line profile in panel (c) apparently shows wing features on both sides, indicating possible gas emission at velocities of about ±350 km s^{-1}. We therefore also fit three Gaussian components simultaneously to the spectrum, shown by the blue curves. The [N II] wing features become weaker from the top-right panel to the bottom-right panel in Figure 3, indicating that the high-velocity [N II] emission is distributed over a wide sky area. Their spatial morphology, shown in panels (c) and (d) in Figure 1, indicates two narrow and long stretches that are apparently reminiscent of tidal tails. The presence of tidal gas tails would firmly establish the on-going galaxy major merger scenario (Toomre & Toomre 1972). However, this requires further observational confirmation as these high-velocity [N II] features are detected only at S/N ≈ 2−3.

The velocities of the [N II] wing components are also indicated for the CO(7−6) and [C I] lines in the left panels in Figure 3. We detect some emission excess on both wings of the main Gaussian fit to the CO(7−6) emission. As our analysis in Section 3.1 shows, this high-velocity CO(7−6) emission is likely associated with the dominant source S, which is probably the host of the QSO.

3. Analysis and Discussion

3.1. CO(7-6) Emission

The FWHM major axis from our 2D Gaussian fit to the CO(7−6) image in Figure 1(g) is $1\farcs34(\pm0\farcs06)$ (at PA = 67° ± 5°), suggesting that the emission is barely resolved

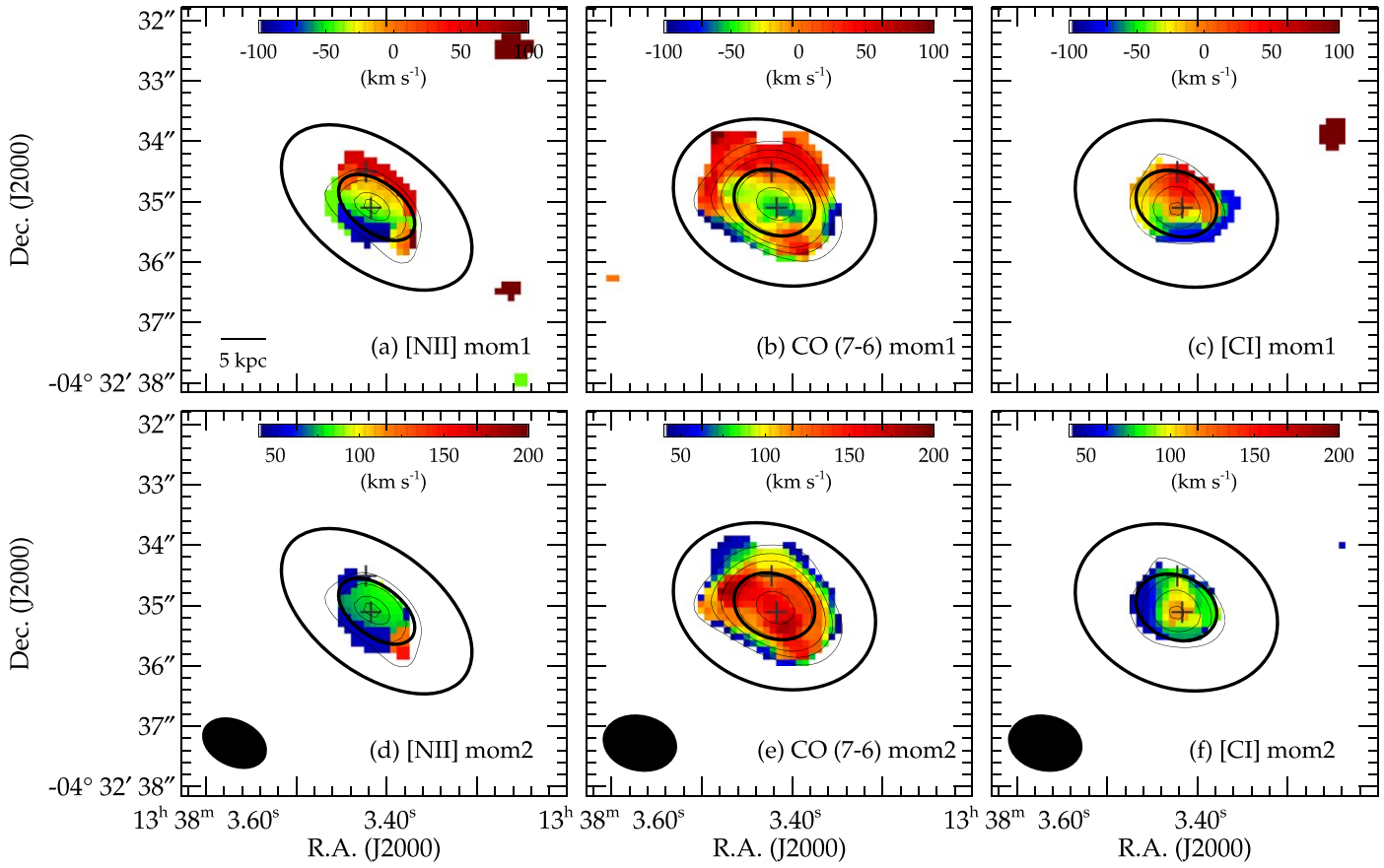

Figure 2. First moment (top row) and second moment (bottom row) images of the [N II], CO(7−6), and [C I] lines, respectively. Only channel pixels (spaxels) above 2.5σ were used in deriving these images, where σ is the rms spaxel-to-spaxel noise. The contours overlaid are that from the corresponding panel in Figure 1. For the [N II] line, the contours that form Figure 1(b) are shown here. For clarity, the same crosses and the elliptical apertures as in Figure 1 are also plotted here, but in thick black lines.

at best. A 2D deconvolution of the source size with the ALMA beam (using the CASA function "deconvolvefrombeam") results in a beam-deconvolved diameter of $d_{\rm deconv} \approx 0\farcs6 \pm 0\farcs1$ (equivalent to 4.1 ± 0.7 kpc) at $\rm PA_{deconv} \approx 44°$. Figure 1(d) shows that the peak surface brightness of the CO(7−6) emission is close to the location of source S, suggesting that this source dominates the CO(7−6) flux.

The peak velocity dispersion of the CO(7−6) emission is $\sim$180 km s^{-1} in Figure 2(e). If one extracts a series of CO(7−6) spectra using apertures of the size index n from 0.5 to 3.0, and fit a Gaussian profile to each spectrum extracted, the resulting line widths show little change as the aperture size increases (see Table 2). This suggests that most of the warm/dense molecular gas should be concentrated within an area smaller than the ALMA beam size.

Given the relatively high S/N obtained for the CO(7−6) emission, we show in Figure 4 six contiguous velocity channel images for this line. Figure 4(a) is from the frequency range where there is an excess emission between the main [C I] and CO(7−6) profiles in Figures 3(a) or (b). The peak emission in Figure 4(a) is significant at $\sim 3.6\sigma$ and appears to be spatially associated with source S. This signal is also clearly detected at a peak S/N $\approx$ 3.9 (3.5) in Figures 3(a) (3(b)) after we remove the two Gaussian line profiles shown. The spectral signal peaks at a velocity of about -500 km s^{-1} with respect to the line center of the CO(7−6) emission. Its velocity width is rather uncertain, but appears to be between 200 and 400 km s^{-1}. This emission could be either from (i) blueshifted CO(7−6) emission or (ii) redshifted [C I] emission, at a maximum velocity of $\sim$600 km s^{-1} if only one of the lines is the dominant contributor. Another possibility is that (iii) blueshifted CO(7−6) and redshifted [C I] emission are both present. In this case, each emission could have a lower maximum velocity. Possibility (ii) is less likely because the redshifted [C I] signal would amount to as much as one-third of the main line peak. Therefore, there should be significant blueshifted CO(7−6) emission regardless of whether (i) or (iii) is the actual case. For the analyses that follow, we assume that (i) is the case for the sake of simplicity.

The individual channel images in Figure 4 also show that the inner emission contours center near source S at all velocities, especially below 80 km s^{-1}. This suggests that source S is indeed the dominant CO(7−6) emitter. Figure 4(f) shows the most redshifted CO(7−6) emission detected at S/N $\gtrsim$ 3. Corresponding to the emission excess seen on the red wing of the main CO(7−6) profile in Figures 3(a) or (b), this redshifted signal peaks spatially at a location only slightly southwest of the position of the most blueshifted CO(7−6) emission in Figure 4(a). Note that any CO(2−1) emission associated with the CO(7−6) line emission in either Figures 4(a) or (b) would be outside the bandwidth of Riechers et al. and therefore is not expected to be seen in their CO(2−1) observations.

The observed spatial locations of the blue and redshifted CO(7−6) emission is suggestive of a possible bipolar gas outflow. The maximum velocity of the blueshifted outflow could be as high as $\sim$600 km s^{-1} although this estimate may be

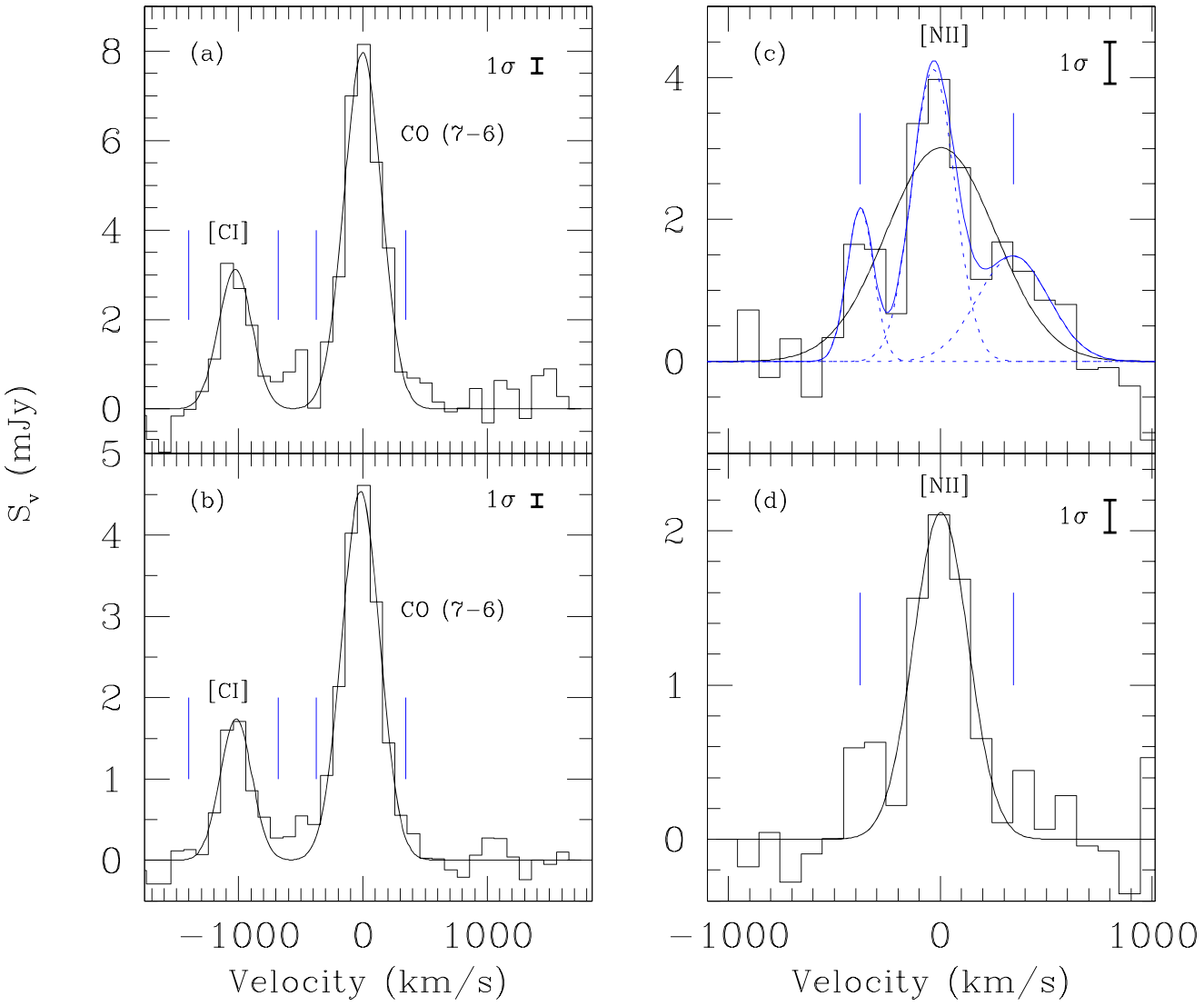

Figure 3. Extracted 1D spectra from the CO(7−6) (left panels) and [N II] (right panels) spectral cubes, respectively, using an elliptical aperture of the size index $n = 2.5$ (upper panels) or $n = 1.0$ (lower panels). The aperture size index n (see the text) is the common stretch factor for the major and minor axes of the aperture relative to the reference ellipse defined by the 2D Gaussian fit to the frequency-integrated line image. The velocity scales are with respect to the CO(7−6) and [N II] line central frequencies (in Table 1), respectively. Therefore, the observed central frequency of the [C I] line is located at -1025 km s^{-1}. The black solid curve in each panel is the best fit to the spectrum using either one or two Gaussian functions assuming zero residual continuum. The blue solid curve in panel (c) is a three-component Gaussian fit to the spectrum with the individual components shown by the dotted curves in blue. For each spectral line, a pair of blue vertical bars mark the velocities of the peaks of the two minor Gaussian components of the [N II] emission in panel (c). The estimated 1σ error bar is shown in each panel.

subject to contamination from any redshifted [C I] emission (see Figure 3(a)). On the red side, the maximum velocity of the outflow could be as high as $\sim$500 km s^{-1}, subject to a considerable uncertainty associated with the relatively low S/N ratios achieved (see Figure 3(a)). Even though gas outflows at velocities ranging from 250 to as high as 1400 km s^{-1} have been claimed in a number of high-z QSOs (e.g., Maiolino et al. 2012; Weiß et al. 2012; Cicone et al. 2015; Feruglio et al. 2017), the confirmation of this possible CO(7−6) gas outflow in BRI 1335-0415 still requires more sensitive observations in the future. Nevertheless, such an outflow should have a minor contribution to the total flux of the CO(7−6) emission (see Figure 3(a)) and a negligible effect on the line width of the Gaussian fit to the main emission profile (see Figure 3(b)).

The CO(7−6) line width given in Table 1 is significantly narrower than, but still consistent (within about 1σ) with, the CO(5−4) line width of 420 ± 60 km s^{-1} given in Guilloteau et al. (1997). However, their spectrum is at significantly lower S/N and has a narrower frequency coverage ($\sim$1100 km s^{-1}) than ours. Using their CO(5−4) line flux, we derived that the CO(7−6)/CO(5−4) luminosity ratio is $\sim$1.3. This ratio suggests a rest frame $C(60/100) > 1$ based on the template CO SLEDs in Lu et al. (2017a; see their Table 6).

The total CO(7−6) flux in Table 1 is 3.08($\pm$0.11) Jy km s^{-1} based on the Gaussian fit to the line profile in Figure 3(a). The total CO(2−1) flux from a VLA D-array observation is 0.62($\pm$0.03) Jy km s^{-1} (Jones et al. 2016). This flux likely represents the total CO(2−1) flux better than the flux of 0.43 Jy km s^{-1} from the higher-resolution observation in Riechers et al. (2008). This translates to a line luminosity ratio of $L_{\rm CO(7-6)}/L_{\rm CO(2-1)} \approx 17.4$. In comparison, the CO(7−6) and CO(2−1) fluxes of Arp 220 are 9.29($\pm$0.19) and 1.27($\pm$0.04) $\times$ 10^{-17} W m^{-2}, respectively (Martín et al. 2011; Lu et al. 2017a), resulting in $L_{\rm CO(7-6)}/L_{\rm CO(2-1)} \approx 7.3$. Therefore, the warm CO emission

Table 2
Gaussian Line Profile: Central Frequency and FWHM[a]

Line (1)	$n = 0.5$ (2)	$n = 1.0$ (3)	$n = 2.0$ (4)	$n = 2.5$ (5)	$n = 3.0$ (6)
CO(7−6)	(149.189, 360)	(149.188 ± 0.002, 360 ± 9)	(149.181, 359)	(149.179 ± 0.003, 354 ± 11)	(149.179, 350)
[C I]	(149.685, 293)	(149.687 ± 0.003, 298 ± 13)	(149.688, 303)	(149.690 ± 0.004, 314 ± 16)	(149.692, 338)
[N II]	(270.236, 280)	(270.237 ± 0.011, 302 ± 26)	(270.241, 471)	(270.238 ± 0.028, 603 ± 64)	(270.237, 694)

Note.
[a] n = the aperture size index. Each pair of numbers in brackets are the line central frequency in GHz and the line FWHM in km s^{-1}, both from a 1D Gaussian line profile fitting. For simplicity, the uncertainties are shown only for the cases of $n = 1.0$ and 2.5.

in BRI 1335-0417 is twice as prominent as that in Arp 220, one of the brightest local (U)LIRGs.

3.2. [C I] 370 μm *Emission*

Like the CO(7−6) emission, the [C I] emission in Figure 1(h) is also barely resolved at best, with $d_{\rm deconv} = 0\farcs7(\pm0\farcs2)$ (equivalent to 5 ± 1 kpc) at $\rm PA_{deconv} \approx 42°$. This $d_{\rm deconv}$ is apparently larger than that for the CO(7−6) emission although the difference is not statistically significant. Our estimated $d_{\rm deconv}$ value of the [C I] emission is comparable to the scale of the CO(2−1) distribution seen in the $0\farcs23$-resolution VLA map in Riechers et al. (2008). This is not unexpected as the [C I] emission in local galaxies scales not only in flux (e.g., Jiao et al. 2017; Lu et al. 2017a), but also in spatial distribution with a low-J CO line emission such as CO(1−0) or CO(2−1) (e.g., Ojha et al. 2001; Ikeda et al. 2002; Beuther et al. 2014).

The extracted 1D spectrum (Figure 3(a)) of the [C I] emission has a peak flux density of 3 mJy (see Figure 3(a)), consistent with the upper flux limit of 5.1 mJy set for this line in Walter et al. (2011). Table 2 shows that the [C I] line velocity width increases moderately with an increasing aperture used for the spectrum extraction. For example, the line FWHM increases by 15% from 293 to 338 km s^{-1} when the aperture size index increases from $n = 0.5$ to $n = 3.0$. Even though the amount of the increase is statistically significant only at 2–3σ, the increase is systematic and more noticeable than that in the CO(7−6) line. This suggests that the spatial distribution of the molecular gas traced by the [C I] line is effectively broader than the denser molecular gas traced by the CO(7−6) line. Furthermore, for the aperture of $n \leqslant 1$, the FWHM of the [C I] line is meaningfully (i.e., at $\gtrsim 4\sigma$) less than that of the CO(7−6) line. This line width difference in the inner region of the galaxy is consistent with the velocity dispersion difference between these lines in Figure 2. Therefore, the gas traced by the [C I] emission is effectively less concentrated toward the galaxy center than the warm dense gas traced by the CO(7−6) emission. Likewise, the ionized gas dominating the [N II] emission distributes over a much larger spatial scale than the molecular gas dominating the [C I] emission.

The observed [C I] flux in Table 1 corresponds to $L' = (1.6 \pm 0.1) \times 10^{10}$ K km s^{-1} pc^2. Using a sample of local (U)LIRGs with both CO(1−0) and [C I] flux measurements, Jiao et al. (2017) showed that there is a nearly linear correlation between the logarithmic line luminosities of the CO(1−0) and [C I] emission, with a scatter of ∼0.19 dex. This observation is the basis for their derivation of a mean relationship between the total molecular gas mass, $M_{\rm gas}$, and the [C I] line luminosity. In practice, since the [C I] line has a modest $T_{\rm ex} \approx 63$ K, its luminosity has a dependence on the gas temperature. To some extent, this systematic effect has been accounted for by the observed scatter around their mean correlation between $M_{\rm gas}$ and the [C I] luminosity, which translates to their claimed uncertainty of a factor of 2−3 in the derived $M_{\rm gas}$. Using their Equation (11), we derived $M_{\rm gas} \approx 4.4 \times 10^{11}\,M_\odot$. This gas mass estimate is only 5 times larger than the molecular gas mass of $9.2 \times 10^{10}\,M_\odot$ estimated by Riechers et al. (2008) based on their CO(2−1) flux and the typical ULIRG CO-to-H_2 mass conversion factor. The difference could be easily accounted for by the differences between the gas mass estimators used (see Jiao et al. 2017) and the fact that our observation used a larger synthesized beam.

For local (U)LIRGs, the ratio $L_{\rm [C\,I]}/L_{\rm CO(7-6)}$ decreases significantly as $C(60/100)$ increases (Lu et al. 2017a). Figure 7 in the Appendix illustrates this correlation using a plot reproduced from Lu et al. (2017a). For BRI 1335-0417, the observed $\log L_{\rm [C\,I]}/L_{\rm CO(7-6)} = -0.47$ (±0.04), which corresponds to $C(60/100) \sim 1.21$ (±0.11) based on the solid line in Figure 7. In comparison, $\log L_{\rm [C\,I]}/L_{\rm CO(7-6)} \approx -0.30$ for Arp 220.

Since $L_{\rm CO(7-6)} \propto$ SFR and $L_{\rm [C\,I]} \propto L_{\rm CO(1-0)}$, the correlation in Figure 7 suggests that the ratio $\rm SFR/L_{CO(1-0)}$ increases by a factor of ∼6 as $C(60/100)$ increases from ∼0.4, which is not too different from the FIR colors for local normal, star-forming galaxies, to 1.2, where most ULIRGs tend to show up. This magnitude of the variation in $\rm SFR/L_{CO(1-0)}$ is roughly what is seen in Genzel et al. (2010; see their Figure 2). Figure 7 shows that the change in $\rm SFR/L_{CO(1-0)}$ is not bi-modal, but a continuous function of $C(60/100)$ (see also Gao & Solomon 2004; Cheng et al. 2018). If $L_{\rm [C\,I]}$ is proportional to $M_{\rm gas}$, the ratio $L_{\rm CO(7-6)}/L_{\rm [C\,I]}$ merely measures the so-called SF efficiency (SFE).

3.3. [N II] 205 μm *Emission*

The [N II] emission appears to be more extended than both CO(7−6) and [C I] emission, and has an FWHM major axis of $1\farcs7(\pm0\farcs3)$ (see Table 1). This leads to $d_{\rm deconv} = 1\farcs3 \pm 0\farcs3$ (or 9 ± 2 kpc) at $\rm PA_{deconv} \approx 44°$. This size is about twice as large as that for the CO(7−6) emission, with the observed size difference at a significance level of ∼2.3σ. The phenomenon that the [N II] emission is much more extended than both of the underlying dust continuum and CO(7−6) emission is also seen in some other high-z galaxies. For example, the [N II] emission is at least twice as extended as the dust continuum emission for both the QSO and SMG in the compact, interacting galaxy group BR 1202-0725 at $z = 4.7$ (Lu et al. 2017b).

It is interesting to notice that the major-axis PA's of all three emission lines, after the deconvolution with the ALMA beam, are around 44°. The PA from the [N II] emission should be

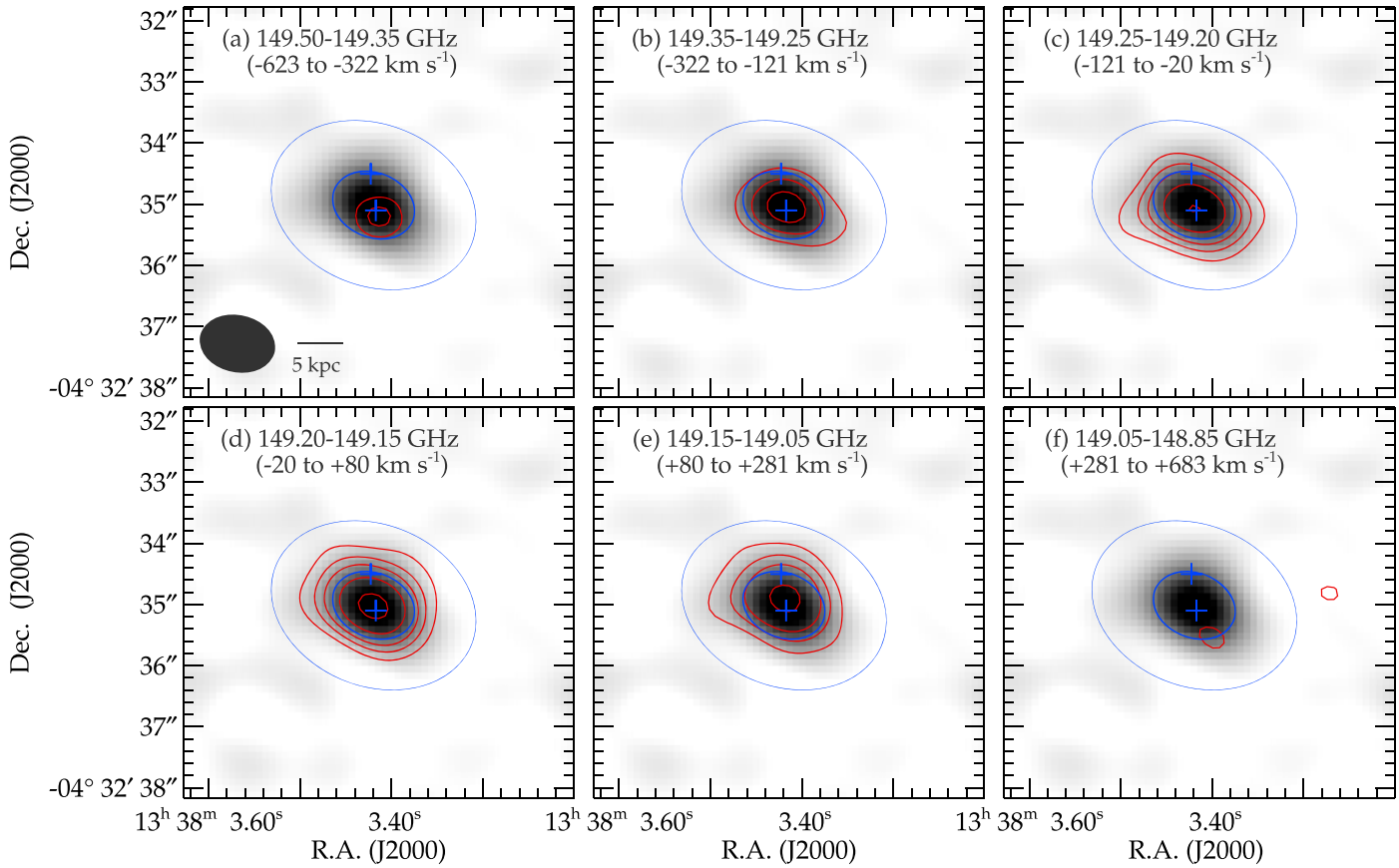

Figure 4. Velocity channel images of the CO(7−6) line emission with the channel frequency and velocity ranges noted in each panel. The gray image is always the total CO(7−6) image from Figure 1(g). Starting at 3× the rms noise and being in units of Jy beam^{-1} km s^{-1}, the contour levels are (a) [3.0, 3.6] × 0.052, (b) [3, 6, 9] × 0.046, (c) [3, 6, 9, 15, 22] × 0.027, (d) [3, 6, 9, 15, 22] × 0.028, (e) [3, 6, 9, 15] × 0.041, and (f) [3.0] × 0.049. The other overplotted symbols are the same as those in Figure 1.

reliable as the line emission is well resolved spatially. This deconvolved PA is not in the direction along sources S and N, but is more aligned with the major axis of source S. This may simply reflect the fact that source S is the dominant one in the system.

The extracted 1D spectrum of the [N II] emission in Figure 3(c) appears to comprise a core component and two fainter, but distinct wing components, albeit with both of them having a peak S/N just below 3. While the brightest part of the blue-wing image is near source S (see Figure 1(c)), that of the red-wing image is in proximity of source N (see Figure 1(d)). This pattern, along with the fact that both wings appear as a long, narrow structure over a projected scale of 15–20 kpc, is reminiscent of tidal gas tails in a galaxy major merger, rather than related to the possible CO(7−6) outflows discussed in Section 3.1, which appear to largely align with the line of sight. However, these [N II] wing components are only detected at S/N ∼ 2–3, the tidal tail picture remains as a speculation at this point.

We also fit 3 Gaussians to the full [N II] spectrum and the best fit is shown by the solid blue curve in Figure 3(c), with the dotted blue curves representing the individual Gaussian components. These Gaussian fits are also given in Table 1. The peaks of the two minor Gaussian components correspond, respectively, to the velocity shifts of −355 and +340 km s^{-1} relative to the main Gaussian peak. In Figure 3, these velocities are marked by the two blue bars for each of the three lines. We note that the reduced chi-squared values are 0.64 and 1.29 for the 3-Gaussian and single-Gaussian fits in Figure 3(c), respectively, indicating that the single Gaussian is statistically a better fit although both fits are not very satisfactory. We also tried a couple of ways to fit the data with 2 Gaussian components. The resulting reduced chi-squared values of ∼1.34 are slightly larger than that for the single-Gaussian fit. We therefore derived two [N II] luminosities in Table 1 from Figure 3(c). One is based on the flux from the single-Gaussian fit to the [N II] spectrum and the other is based on the flux of the central Gaussian component in the 3-Gaussian component fit. We use these, respectively, as the upper and lower limits on the true [N II] luminosity in our line luminosity ratio analysis below.

3.4. Line Luminosity Ratios and FIR Dust Emission

The continuum fluxes at $\lambda_{\rm obs} \approx 1108$ and 2011 μm measured in this work are shown in Figure 5, along with other published fluxes at various wavelengths. The solid curve in Figure 5 is the best graybody spectral energy distribution (SED) fit to all the data points with a fixed dust emissivity power-law index $\beta = 1.8$ (Planck Collaboration et al. 2011). This SED fit gives $T_{\rm dust} = 41.5$ K or $C(60/100) \approx 1.1$.

We also used various line luminosity ratios to estimate the value of $C(60/100)$ using the luminosity values calculated in Table 1. The resulting estimates of $C(60/100)$ are summarized in Table 3 and range from ∼1.05 to ∼1.20, with a typical uncertainty of 0.10 or 0.15 in each estimate. The average value

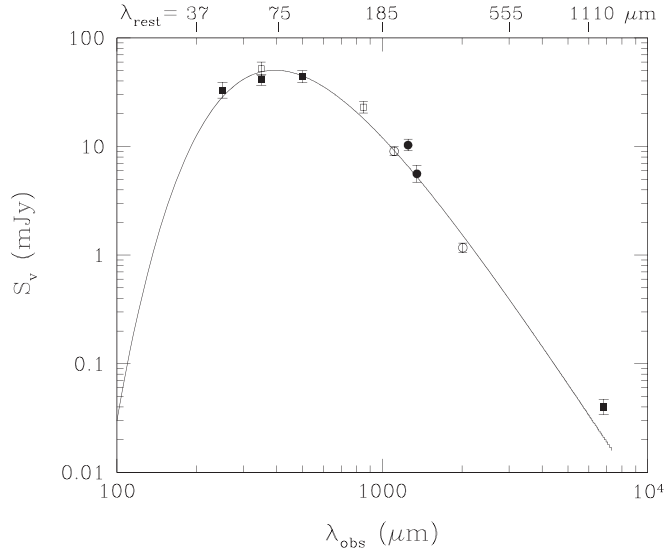

Figure 5. Plot of continuum flux measurements as a function of the observed wavelength. (The corresponding range of the rest-frame wavelength is indicated on the top.) Different symbols indicate the sources of the data: filled squares (Wagg et al. 2014), open squares (Benford et al. 1999), open circles (this work), and filled circles (Guilloteau et al. 1997). The solid curve is the best graybody SED fit (with a fixed power-law emissivity index $\beta = 1.8$) to the data based on an equal weight basis, yielding $T_{\rm dust} = 41.5$ K.

of 1.1 ($\pm$0.1) for $C(60/100)$ corresponds to $T_{\rm dust} \approx 41$ ($\pm$2)K if β is also fixed at 1.8. This temperature estimate is in good agreement with that from the direct SED fit.

The FIR (42−122 μm) luminosity, $L_{\rm FIR}$, is $1.9 \times 10^{13}\,L_\odot$ from the SED fit in Figure 5, resulting in $\log L_{\rm CO(7-6)}/L_{\rm FIR} \approx -4.46$. This value is within $\sim 1.2\sigma_s$ of the average value of this ratio for the local SF-dominated LIRGs in Lu et al. (2015), where σ_s is the local sample standard deviation. This result confirms that the CO(7−6) emission in the QSO BRI 1335-0417 is an excellent SFR predictor and that the FIR luminosity is also dominated by the SF in this QSO.

3.5. Star Formation and Gas Properties

Following Lu et al. (2015), the SFR inferred from $L_{\rm CO(7-6)}$ is $5.1 \times 10^3\,M_\odot\,{\rm yr}^{-1}$ using the initial mass function (IMF) of Chabrier (2003). For local (U)LIRGs, $\Sigma_{\rm SFR}$ is empirically correlated with the rest frame $C(60/100)$ (Liu et al. 2015) or $f_\nu(70\,\mu{\rm m})/f_\nu(160\,\mu{\rm m})$ (Lutz et al. 2016). The scatter of these correlations is still fairly significant, e.g., ~0.6 dex in Lutz et al. (2016). Nevertheless, these two independent correlations, together with the flux densities from our SED fit, give comparable estimates of $\Sigma_{\rm SFR} \sim 1 \times 10^3\,M_\odot\,{\rm yr}^{-1}\,{\rm kpc}^{-2}$ after adjusting them to Chabrier IMF and increasing the $L_{\rm FIR}$-based SFR in Lutz et al. by a factor of 2 to align with the Kennicutt (1998) formula. These estimates of $\Sigma_{\rm SFR}$ are quite high, approaching the Eddington limit on the order of $10^3\,M_\odot\,{\rm yr}^{-1}\,{\rm kpc}^{-2}$ (Murray et al. 2005; Thompson et al. 2005; Hopkins et al. 2010).

The face-on FWHM diameter, $d_{\rm SF}$, of the SF region is estimated to be $1.7^{+1.7}_{-0.8}$ kpc, via $\Sigma_{\rm SFR} = (\frac{1}{2}\,{\rm SFR})/(\frac{1}{4}\pi\,d_{\rm SF}^2)$. While this estimated $d_{\rm SF}$ is smaller than the deconvolved diameter of $d_{\rm deconv} = 4.1 \pm 0.7$ kpc from the image analysis of the CO(7−6) emission, the difference is only significant at $\sim 1.3\sigma$. Following Scoville et al. (2016), we also derived $M_{\rm gas} \approx 5 \times 10^{11}\,M_\odot$ based on the rest frame $f_\nu(850\,\mu{\rm m})$ from our continuum SED fit. The formal uncertainty for this $M_{\rm gas}$ estimate is about a factor of 2. This is in good agreement with the molecular gas mass inferred from our [C I] flux above. The characteristic gas depletion time $\tau_{\rm gas}$ ($\equiv M_{\rm gas}/{\rm SFR}$) is $\sim 10^8$ years.

The derived SFR of $5.1 \times 10^3\,M_\odot\ {\rm yr}^{-1}$ for BRI 1335-0417 is similar to that of the QSO and SMG in the BR 1202-0725 galaxy group system at $z = 4.7$ (Lu et al. 2017b), making BRI 1335-0417 one of the high-z galaxies with the highest SFR known. Among the brightest ULIRGs in the local universe, Arp 220 has $L_{\rm CO(7-6)} \approx 2.2 \times 10^7\,L_\odot$ and $L_{\rm [C\,I]} \approx 1.1 \times 10^7\,L_\odot$ (Lu et al. 2017a). Therefore, the $L_{\rm CO(7-6)}$-based SFR and $L_{\rm [C\,I]}$-base $M_{\rm gas}$ ratios of BRI 1335-0417 to Arp 220 are ~35 and ~24, respectively. The ratio of these two values is ~1.5, which implies a 50% larger SFE for BRI 1335-0417.

Table 3
Line Luminosity Ratio

Line Luminosity Ratio (1)	Value (2)	$C(60/100)$[a] (3)	References[b] (4)
$\log$ ([N II]$_{\rm core}$/CO(7−6))	−0.21($\pm$0.06)[c]	1.20 ($\pm$0.15)	(1)
$\log$ ([N II]$_{\rm total}$/CO(7−6))	+0.06($\pm$0.06)[c]	1.06 ($\pm$0.15)	(1)
$\log$ ([C II]/CO(7−6))	+1.30($\pm$0.09)[c]	1.04 ($\pm$0.15)	(1)
$\log$ ([C I]/CO(7−6))	−0.47($\pm$0.04)[d]	1.20 ($\pm$0.11)	(2, 3)
CO(7−6)/CO(5−4)[e]	+1.30($\pm$0.15)[c]	>1.0	(2)

Notes.
[a] The uncertainty is dominated by the scatter of the line ratios of the local calibration sample, i.e., 0.1 to 0.15.
[b] References for converting a line luminosity ratio to $C(60/100)$: (1) Lu et al. (2015); (2) Lu et al. (2017a); (3) Appendix of this work.
[c] The uncertainty calculated assumes a total flux uncertainty of 10% for the line flux measured in this work.
[d] The uncertainty given here is free from any ALMA systematic flux calibration error.
[e] The CO(5−4) flux is taken from Guilloteau et al. (1997).

3.6. On Merger-induced SF at High z

In Figure 6, we compare BRI 1335-0417 and a few other high-z ULIRGs with the local (U)LIRG sample in Lu et al. (2015) via plots, all as a function of $C(60/100)$ (left panels) or $\log L_{\rm FIR}$ (right panels), of $\log L_{\rm [C\,II]}/L_{\rm CO(7-6)}$ (two top panels), $\log L_{\rm [N\,II]}/L_{\rm CO(7-6)}$ (middle panels) and $\log d_{\rm SF}$ (bottom panels). The $d_{\rm SF}$ values are derived from the $L_{\rm FIR}$-based SFR and $C(60/100)$-based $\Sigma_{\rm SFR}$ as prescribed in Lu et al. (2015). That is, $\log d_{\rm SF} = 0.5 \log L_{\rm FIR} - 5.04 \log C(60/100) - 6.17$. The error bars for these $d_{\rm SF}$ estimates are on the order of a factor of 2. All high-z galaxies plotted here have a $C(60/100)$ derived from the FIR dust SED fitting and their $L_{\rm FIR}$ corrected for a gravitational lensing magnification factor when appropriate (see Carilli & Walter 2013).

Despite the fact that some of the high-z galaxies in Figure 6 are an order of magnitude brighter in $L_{\rm FIR}$ than the brightest local ULIRGs, the local and high-z galaxies appear to follow the same average correlation in each of the two top-left panels in Figure 6. On the other hand, clear segregations are seen between the local and high-z galaxies in the two top-right panels in Figure 6. This suggests clearly that it is $C(60/100)$ or $\Sigma_{\rm SFR}$, *rather than* $L_{\rm FIR}$, that drives these line flux ratios. Therefore, a plot of $\log L_{\rm [C\,II]}/L_{\rm FIR}$ (where $L_{\rm FIR}$ can be substituted by $L_{\rm CO(7-6)}$) against $L_{\rm FIR}$ offers diminished diagnostic value in spite of the fact that such plots have been

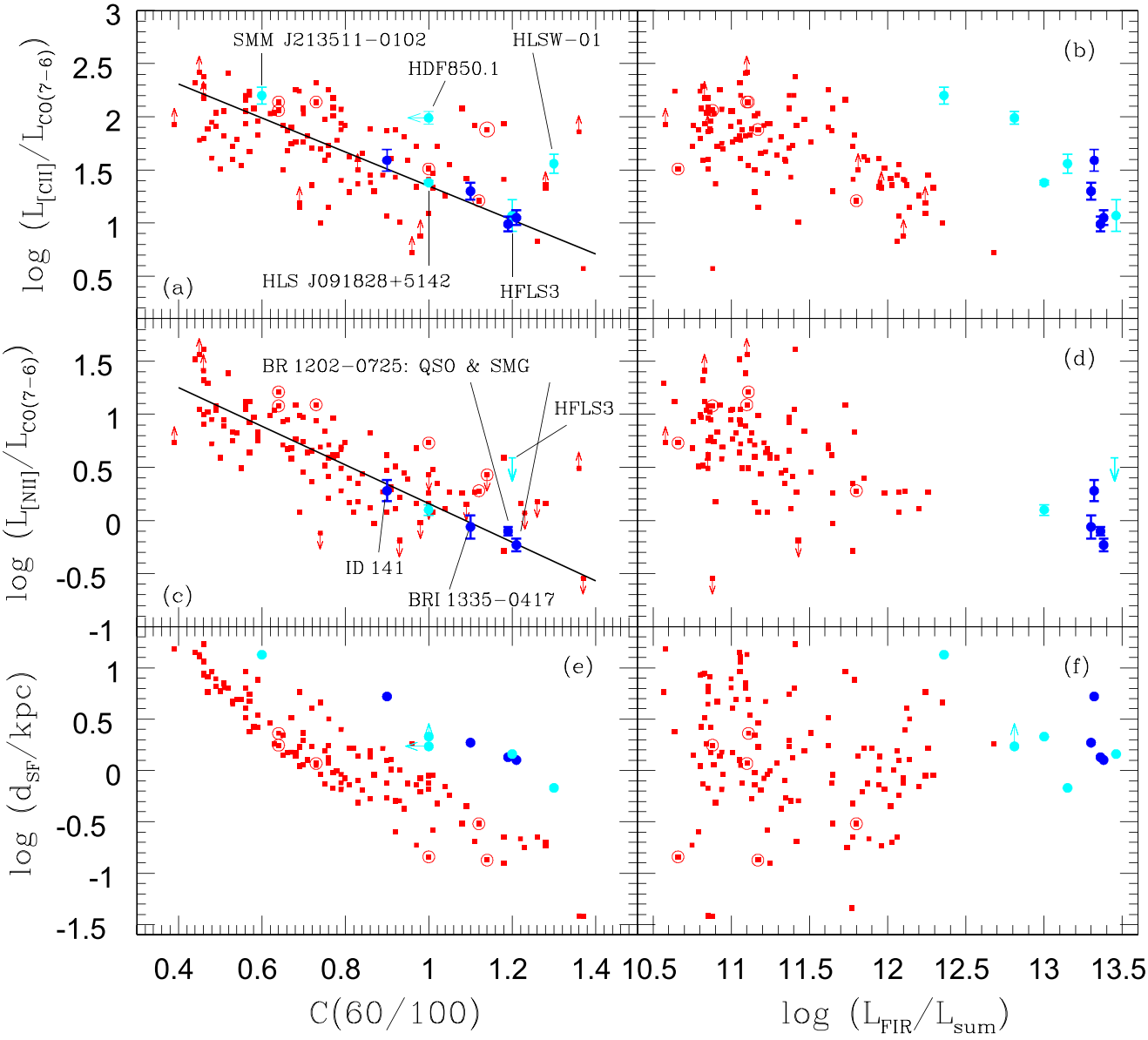

Figure 6. Plots of $\log L_{[\mathrm{C\,II}]}/L_{\mathrm{CO}(7-6)}$ (top panels), $\log L_{[\mathrm{N\,II}]}/L_{\mathrm{CO}(7-6)}$ (middle panels), and $\log d_{\mathrm{SF}}$ (bottom panels) as a function of the FIR color (left panels) or $\log L_{\mathrm{FIR}}$ (right panels), for the local (U)LIRG sample (filled squares in red) and a number of distant ULIRGs at $2 < z < 6.5$ (filled circles in cyan or blue) from Lu et al. (2015), which also has an explanation for the labeling of the high-z galaxies here. The data points further circled in red are the local (U)LIRGs, for which the AGN contribution is likely to dominate the bolometric luminosity based on a number of mid-IR diagnostics (see Lu et al. 2015). Those high-z targets that are also in our ALMA program are plotted in blue (Lu et al. 2017b; and this work), including ID 141 for which we used $C(60/100)$ and L_{FIR} from Cox et al. (2011), a gravitational demagnification factor of 4.1 from Brussmann et al. (2012) and our own [N II] line flux measurement in C. Cheng et al. (2018, in preparation). The solid lines in (a) and (c) represent the average correlation of the local sample given in Lu et al. (2017b). The value of d_{SF} is derived from the L_{FIR}-based SFR and $C(60/100)$ as prescribed in Lu et al. (2015) and has an uncertainty of about a factor of 2.

widely used in the literature for galaxy samples across different redshift epochs.

Furthermore, the two bottom panels in Figure 6 reveal that, with SFR surface densities comparable to that of local ULIRGs, high-z hyperluminous infrared galaxies, such as BRI 1335-0417, reach their higher global SFR mainly via a larger star-forming area. This is in agreement with a similar conclusion reached by Rujopakarn et al. (2011) who estimated Σ_{SFR} based on a radio continuum size in galaxies up to $z \sim 2.5$. The phenomenon that the high-z luminous galaxies have a larger SF area when compared with local ULIRGs is one of the motivations behind the so-called cold gas accretion scenario as the main SF mode for most of the SMGs at high z (e.g., Agertz et al. 2009; Dekel et al. 2009; Davé et al. 2010), as opposed to the merger-triggered SF scenario (e.g., Tacconi et al. 2006, 2008). In the case of BRI 1335-0417, our observational results favor a merger-induced SF scenario. These include (a) the very warm FIR color of $C(60/100) > 1$, (b) the CO(7−6) emission is spatially more compact than the [C I] emission, and (c) a significantly different velocity dispersion between the CO(7−6) and [C I] in the inner region of the galaxy. Together, they suggest that the multiple gas phases traced by these lines arise effectively from different physical regions. Taking into consideration the much larger

spatial scale of the [N II] emission observed, our results appear to agree with the predictions from cosmological simulations on galaxy mergers (e.g., Sparre & Springel 2016).

It is possible that many of the other high-z galaxies with a warm FIR color could also be mergers, e.g., both the SMG and QSO in the BR 1202-0725 system (Lu et al. 2017b) also plotted in Figure 6. These galaxy systems might be caught near the maximum SFR phase of a non-head-on major galaxy merger, which starts before the two progenitors coalesce (e.g., Sparre & Springel 2016). This could make the apparent SF size larger than that in a head-on galaxy merger in which the maximum SF phase occurs when the two galaxy nuclei coalesce. Local examples might be the Antennae Galaxies (Wang et al. 2004) or those widely separated ULIRGs (Dinh-V-Trung et al. 2001). However, the higher gas content in high-z galaxies could lead to a merger-triggered $\Sigma_{\rm SFR}$ much higher than that in the Antennae system. In fact, the inferred values of $\Sigma_{\rm SFR}$ for BRI 1335-0417 and the two ULIRGs in BR 1202-0725 (Lu et al. 2017b) all approach the Eddington limit. Detailed analyses of local ULIRGs also indicate that some of the advanced mergers in the local universe have a $\Sigma_{\rm SFR}$ near the Eddington limit, but with a much smaller SF area (Barcos-Muñoz et al. 2017). This might naturally explain the comparable $C(60/100)$ (or $\Sigma_{\rm SFR}$) values in both local ULIRGs and many of the high-z galaxies in Figure 6. In such a frame work, a head-on galaxy merger would easily trigger a super Eddington $\Sigma_{\rm SFR}$ that could plausibly disrupt or end the starburst in a few million years, giving birth to a post-starburst galaxy. It would be interesting to explore whether the above conjecture may play a significant role in explaining the observations that there is already a population of post-starburst galaxies at $z > 4$ (e.g., Wiklind et al. 2008; Fontana et al. 2009; Richard et al. 2011; Straatman et al. 2014; Decarli et al. 2017). It is not quite intuitive to see why cold gas accretion would stop in these quiescent galaxies, but not the other SMGs at the same redshift epoch, under the orderly rotating disk SF scenario.

4. Summary

We presented our recent ALMA observations of the CO(7−6), [C I] 370 μm, and [N II] 205 μm line emission of BRI 1335-0417, an infrared hyperluminous quasar at $z = 4.407$, which is likely a major merger between two galaxies (N and S) based on previous high-resolution CO(2−1) imaging. Our main results can be summarized as follows:

At the achieved resolutions of $\sim$1.″1 to 1.″2 (or 7.5 to 8.2 kpc), the continuum emission at 205 and 372 μm (rest frame), the CO(7−6), and the [C I] emission are all barely resolved at best. On the other hand, the [N II] emission is clearly resolved with a (FWHM) Gaussian major axis $d_{\rm deconv} = 9 \pm 2$ kpc after a deconvolution with the ALMA beam.

The observed CO(7−6) emission not only confirms that source S dominates the SFR, but also reveals a complicated dynamics for the dense molecular gas. This includes a possible bipolar outflow with a maximum velocity as high as 500 to 600 km s^{-1}, likely driven by the QSO in source S.

While the three lines display similar large-scale velocity fields, they show different velocity dispersion fields: the CO(7−6) line displays a patchy velocity dispersion field with a peak dispersion of $\sim$180 km s^{-1}; the [C I] and [N II] lines display smoother velocity dispersion fields, reaching a peak value of only $\sim$120 and $\sim$80 km s^{-1}, respectively. This suggests that the three lines arise effectively from different regions, a picture that fits better with a merger-trigger SF scenario than with an orderly rotating disk SF scenario.

The far-infrared (FIR) dust temperature ($T_{\rm dust}$) of 41.5 K from the graybody fit to the continuum measurements agrees well with the average $T_{\rm dust}$ inferred from the line luminosity ratios of $L_{\rm [N\,II]}/L_{\rm CO(7-6)}$, $L_{\rm [C\,II]}/L_{\rm CO(7-6)}$, and $L_{\rm [C\,I]}/L_{\rm CO(7-6)}$. The resulting $L_{\rm CO(7-6)}/L_{\rm FIR}$ is consistent with that of the SF-dominated luminous infrared galaxies in the local universe, thus confirming the validity of using $L_{\rm CO(7-6)}$ as an SFR tracer for such high-z dusty QSOs. We estimated an SFR of $5.1(\pm1.5) \times 10^3\,M_\odot\,{\rm yr}^{-1}$ (assuming the Chabrier IMF), an effective diameter of $1.7^{+1.7}_{-0.8}$ kpc for the SF region, a near Eddington-limit SFR surface density of $\sim 1 \times 10^3\,M_\odot\,{\rm yr}^{-1}\,{\rm kpc}^{-2}$, and a molecular gas mass of $\sim 5 \times 10^{11}\,M_\odot$.

We show quantitative evidence that, with SFR surface densities comparable to that of local ULIRGs, high-z hyperluminous infrared galaxies, such as BRI 1335-0417, reach their higher global SFR mainly via a larger star-forming area.

We thank an anonymous referee for a number of helpful comments. This paper makes use of the following ALMA data: ADS/JAO.ALMA#2015.1.00388.S. ALMA is a partnership of ESO (representing its member states), NSF (USA), and NINS (Japan), together with NRC (Canada), NSC and ASIAA (Taiwan), and KASI (Republic of Korea), in cooperation with the Republic of Chile. The Joint ALMA Observatory is operated by ESO, AUI/NRAO, and NAOJ. This work is supported in part by the National Key R&D Program of China grant #2017YFA0402704, the NSFC grant #11673028, and the Chinese Academy of Sciences (CAS), through a grant to the CAS South America Center for Astronomy (CASSACA) in Santiago, Chile. C.C. is supported by CAS through the CASSACA postdoc and visiting scholarship grant administered by the CASSACA, NAOC.

Appendix
[C I] to CO (7−6) Luminosity Ratios of Local LIRGs

Figure 7 is a reproduction of Figure 17(c) in Lu et al. (2017a). We carried out least-squares fits to all the data points with both CO(7−6) and [C I] lines detected, excluding the seven AGN-dominant LIRGs (circled in red) and NGC 6240 (circled in blue). The least-squares bisector (Isobe et al. 1990) result, given in Equation (1), is shown by the solid line. The scatter around the fit is equivalent to 0.11 in terms of $C(60/100)$.

$$\log L_{\rm [C\,I]}/L_{\rm CO(7-6)} = (0.74 \pm 0.05) - (1.00 \pm 0.06)\,C(60/100). \quad (1)$$

The large cross in magenta in the plot is the location of BRI 1335-0417 from this study, using the measured [C I]/CO(7−6) luminosity ratio and the $C(60/100)$ value from the SED fit. The horizontal error bar indicates the possible range for its $C(60/100)$ value. Most of the local AGN-dominant LIRGs lie above the solid line. This is likely due to the fact that the CO(7−6) emission is rather insensitive to AGN gas heating (Lu et al. 2017a).

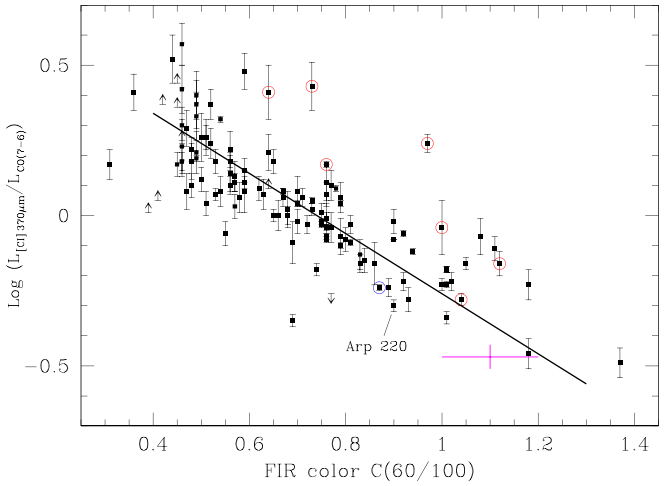

Figure 7. Plot of $\log L_{[\mathrm{C\,I}]}/L_{\mathrm{CO}(7-6)}$ as a function of $C(60/100)$ for a flux-limited local sample of LIRGs (filled squares), adopted from Figure 17 in Lu et al. (2017a). The data points circled in red are the galaxies, for which the AGN contribution is likely to dominate the bolometric luminosity based on a number of mid-IR diagnostics, and the data point circled in blue is NGC 6240 where there is significant gas heating by shocks unrelated to star formation (see Lu et al. 2017a for further details). The solid line is a bisector least-squares fit to all the data points detected in both [C I] and CO(7−6), excluding those circled. The data point in magenta represents BRI 1335-0417 from this study, with its horizontal error bar corresponding to the possible range of the $C(60/100)$ value. Also labeled is Arp 220, one of the brightest local (U)LIRGs.

ORCID iDs

Nanyao Lu https://orcid.org/0000-0002-8948-1044
Tianwen Cao https://orcid.org/0000-0002-1335-6212
George C. Privon https://orcid.org/0000-0003-3474-1125
David B. Sanders https://orcid.org/0000-0002-1233-9998

References

Agertz, O., Teyssier, R., & Moore, B. 2009, MNRAS, 397, L64
Bañados, E., Venemans, B. P., Mazzucchelli, C., et al. 2018, Natur, 553, 473
Barcos-Muñoz, L., Leroy, A. K., Evans, A. S., et al. 2017, ApJ, 843, 117
Barnes, J., & Hernquist, L. 1996, ApJ, 471, 115
Benford, D. J., Cox, P., Omont, A., et al. 1999, ApJL, 518, L65
Beuther, H., Ragan, S. E., Ossenkopf, V., et al. 2014, A&A, 571, A53
Blain, A. W., Smail, I., Ivison, R., et al. 2002, PhR, 369, 111
Bournaud, F., Powell, L. C., Chapon, D., & Teyssier, R. 2011, in IAU Symp. 271, Astrophysical Dynamics: From Stars to Galaxies, ed. N. Brummell et al. (Cambridge: Cambridge Univ. Press), 160
Brussmann, R. S., Gurwell, M. A., Fu, H., et al. 2012, ApJ, 756, 134
Carilli, C. L., Kohno, K., Kawabe, R., et al. 2002, ApJ, 123, 1838
Carilli, C. L., Menten, K. M., & Yun, M. S. 1999, ApJL, 521, L25
Carilli, C. L., & Walter, F. 2013, ARA&A, 51, 105
Casey, C. M., Narayanan, D., & Cooray, A. 2014, PhR, 541, 45
Chabrier, G. 2003, PASP, 115, 763
Cheng, C., Ibar, E., Hughes, T. M., et al. 2018, MNRAS, 475, 248
Cicone, C., Maiolino, R., Gallerani, S., et al. 2015, A&A, 574, A14
Condon, J. J. 1997, PASP, 109, 166
Cox, P., Krips, M., Neri, R., et al. 2011, ApJ, 740, 63
Davé, R., Finlator, K., Oppenheimer, B. D., et al. 2010, MNRAS, 404, 1355
Decarli, R., Walter, F., Venemans, B. P., et al. 2017, Natur, 545, 457
Dekel, A., Birnboim, Y., Engel, G., et al. 2009, Natur, 457, 451
Díaz-Santos, T., Armus, L., Charmandaris, V., et al. 2017, ApJ, 846, 32
Dinh-V-Trung, Lo, K. Y., Kim, D.-C., Gao, Y., & Gruendl, R. A. 2001, ApJ, 556, 141
Downes, D., & Solomon, P. M. 1998, ApJ, 507, 615
Evans, A. S., Mazzarella, J. M., Surace, J. A., & Sanders, D. B. 2002, ApJ, 580, 749
Feruglio, C., Ferrara, A., Bischetti, M., et al. 2017, A&A, 608, A30
Finkelstein, S. L., Papovich, C., Dickinson, M., et al. 2013, Natur, 502, 524
Fontana, A., Santini, P., Grazian, A., et al. 2009, A&A, 501, 15
Gao, Y., & Solomon, P. M. 1999, ApJL, 512, L99
Gao, Y., & Solomon, P. M. 2004, ApJ, 606, 271
Genzel, R., Tacconi, L. J., Gracia-Carpio, J., et al. 2010, MNRAS, 407, 2091
Guilloteau, S., Omont, A., McMahon, R. G., Cox, P., & Petitjean, P. 1997, A&A, 328, L1
Hopkins, P. F., Cox, T. J., Younger, J. D., & Hernquist, L. 2009, ApJ, 691, 1168
Hopkins, P. F., Murray, N., Quataert, E., & Thompson, T. A. 2010, MNRAS, 401, L19
Hu, W., Wang, J., & Zheng, Z.-Y. 2017, ApJ, 845, 16
Ikeda, M., Oka, T., Tatematsu, K., Sekimoto, Y., & Yamamoto, S. 2002, ApJS, 139, 467
Isobe, T., Feigelson, E. D., Akritas, M. G., & Babu, G. J. 1990, ApJ, 364, 104
Jiao, Q., Zhao, Y., Zhu, M., et al. 2017, ApJL, 840, L18
Jones, G. C., Carilli, C. L., Momjian, E., et al. 2016, ApJ, 830, 63
Kennicutt, R. C., Jr. 1998, ARA&A, 36, 189
Lenz, D. D., & Ayres, T. R. 1992, PASP, 104, 1104
Liu, L., Gao, Y., & Greve, T. R. 2015, ApJ, 805, 31
Lu, N., Zhao, Y., Díaz-Santos, T., et al. 2017a, ApJS, 230, 1
Lu, N., Zhao, Y., Díaz-Santos, T., et al. 2017b, ApJL, 842, L16
Lu, N., Zhao, Y., Xu, C. K., et al. 2014, ApJL, 787, L23
Lu, N., Zhao, Y., Xu, C. K., et al. 2015, ApJL, 802, L11
Lutz, D., Berta, S., Contursi, A., et al. 2016, A&A, 591, A136
Maiolino, R., Gallerani, S., Neri, R., et al. 2012, MNRAS, 425, L66
Martín, S., Krips, M., Martín-Pintado, J., et al. 2011, A&A, 527, A36
Murray, N., Quataert, E., & Thompson, T. A. 2005, ApJ, 618, 569
Ojha, R., Stark, A. A., Hsieh, H. H., et al. 2001, ApJ, 548, 253
Omont, A., McMahon, R. G., Cox, P., et al. 1996, A&A, 315, 1
Papadopoulos, P. P., & Greve, T. R. 2004, ApJ, 615, 29
Papadopoulos, P. P., Thi, W.-F., & Witi, S. 2004, MNRAS, 351, 147
Planck Collaboration, Abergel, A., Ade, P. A. R., et al. 2011, A&A, 536, A25
Richard, J., Kneib, J.-P., Ebeling, H., et al. 2011, MNRAS, 414, L31
Riechers, D. A., Walter, F., Carilli, C. L., et al. 2008, ApJL, 686, L9
Rujopakarn, W., Rieke, G. H., Eisenstein, D. J., & Juneau, S. 2011, ApJ, 726, 93
Sanders, D. B., & Mirabel, I. F. 1996, ARA&A, 34, 749
Sanders, D. B., Soifer, B. T., Elias, J. H., et al. 1988, ApJ, 325, 74
Scoville, N. Z., Sanders, D. B., Sargent, A. I., et al. 1989, ApJL, 345, L25
Scoville, N. Z., Sheth, L. K., Aussel, H., et al. 2016, ApJ, 820, 83
Shields, G. A., Menezes, K. L., Massart, C. A., & Vanden Bout, P. 2006, ApJ, 641, 683
Solomon, P. M., Downes, D., Radford, S. J. E., & Barrett, J. W. 1997, ApJ, 478, 144
Solomon, P. M., & Sage, L. J. 1988, ApJ, 334, 613
Sparre, M., & Springel, V. 2016, MNRAS, 462, 2418
Storrie-Lombardi, L. J., McMahon, R. G., Irwin, M. J., & Hazard, C. 1994, ApJL, 427, L13
Storrie-Lombardi, L. J., McMahon, R. G., Irwin, M. J., & Hazard, C. 1996, ApJ, 468, 121
Straatman, C. M. S., Labbé, I., Spitler, L. R., et al. 2014, ApJL, 783, L14
Tacconi, L. J., Genzel, R., Smail, I., et al. 2008, ApJ, 680, 246
Tacconi, L. J., Neri, R., Chapman, S. C., et al. 2006, ApJ, 640, 228
Thompson, T. A., Quataert, E., & Murray, N. 2005, ApJ, 630, 167
Toomre, A., & Toomre, J. 1972, ApJ, 178, 623
Venemans, B. P., Walter, F., Decarli, R., et al. 2017, ApJ, 837, 146
Wagg, J., Carilli, C. L., Aravena, M., et al. 2014, ApJ, 783, 71
Wagg, J., Carilli, C. L., Wilner, D. J., et al. 2010, A&A, 519, L1
Walter, F., Weib, A., Downes, D., Decarli, R., & Henkel, C. 2011, ApJ, 730, 18
Wang, Z., Fazio, G. G., Ashby, M. L. N., et al. 2004, ApJS, 154, 193
Watson, D., Christensen, L., Knudsen, K. K., et al. 2015, Natur, 519, 327
Weiß, A., Walter, F., Downes, D., et al. 2012, ApJ, 753, 102
Wiklind, T., Dickinson, M., Ferguson, H. C., et al. 2008, ApJ, 676, 781
Wootten, A., & Thompson, A. R. 2009, IEEEP, 97, 1463
Xu, C. K., Cao, C., Lu, N., et al. 2014, ApJ, 787, 48
Xu, C. K., Cao, C., Lu, N., et al. 2015, ApJ, 799, 11
Yun, M. S., Carilli, C. L., Kawabe, R., et al. 2000, ApJ, 528, 171
Zhao, Y., Lu, N., Xu, C., et al. 2016a, ApJ, 820, 118
Zhao, Y., Lu, N., Xu, C., et al. 2016b, ApJ, 819, 69